

Supplementary information for article:
**Revealing viscoelastic bending relaxation dynamics of isolated
semiflexible colloidal polymers**

Simon G. Stuij,¹ Hannah J. Jonas,² Zhe Gong,³ Stefano Sacanna,³

Thomas E. Kodger,⁴ Peter G. Bolhuis,² and Peter Schall¹

*¹Institute of Physics, University of Amsterdam,
Science Park 904, 1098 XH Amsterdam, the Netherlands*

*²van 't Hoff Institute for Molecular Sciences,
University of Amsterdam, Science Park 904,
1098 XH Amsterdam, the Netherlands*

*³Molecular Design Institute, Department of Chemistry,
New York University, 29 Washington Place, New York 10003, USA*

*⁴Physical Chemistry and Soft Matter,
Wageningen University, Stippeneng 4,
6708 WE Wageningen, The Netherlands*

I. PATCH SIZE AND PATCH CURVATURE DETERMINATION

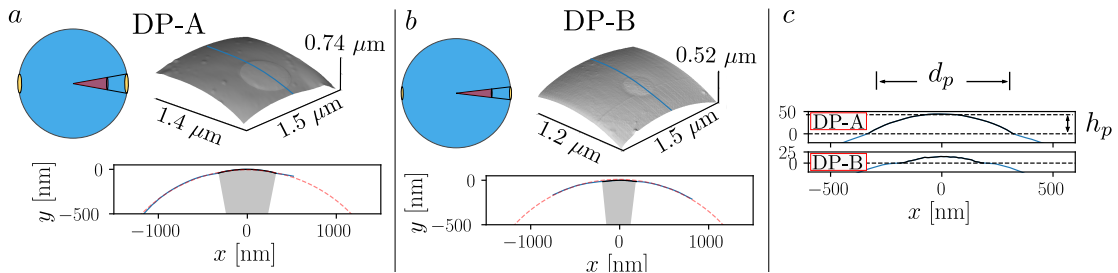


FIG. 1. AFM measurements of the particle patches. (a) Large-patch dipatch particles (DP-A): Schematic indicating definition of projected patch diameter d_p and patch arc angle θ_p , surface height measured using AFM (zoom on patch) and height profile along the blue line indicated in the surface plot. (b) Small-patch dipatch B particles (DP-B) (c) Height profile zoomed in on patch, aspect ratio between x and y is set to 2.

We determined the average patch size of each particle type using a setup that combines optical and atomic force microscopy (AFM), as described in ref. [1]. We quantified the patch size in terms of the patch arc angle θ_p , which is a particle size independent measurement of the patch size, see the schematic in Fig. 1(a,b). The patch arc angle was determined from the projected patch diameter d_p and particle diameter d using the relation $\theta_p = 2 \sin^{-1}(d_p/d)$, see table I(third column). Here, the uncertainty is the standard deviation of the measured patches and gives the patch size polydispersity. We note that the polydispersity is a rough estimation limited by the low measurement statistics.

Apart from patch sizes, the AFM measurements also provide information on the height h_p of the patches. Not all patches stick out equally, as shown by the profiles that are zoomed-in on the patch (Fig. 1c). This results in a different curvature at the patch than for the rest of the particle. Modelling the patches as spherical caps, we can extract the radius of curvature R of each patch via $R = ((d_p/2)^2 + h_p^2) / 2h_p$, see table I. Next to patch size, the patch curvature will influence the inter-patch interaction, as a higher curvature results in less contact when patches are close together and is therefore expected to decrease the interaction strength.

Particle type	d [μm]	d_p [μm]	θ_p [$^\circ$]	h_p [nm]	R_p [μm]
DP-A	3.2(1)	0.58(5)	21(2)	45(5)	1.0(2)
DP-B	3.1(1)	0.38(5)	14(2)	15(5)	1.2(2)

TABLE I. Patchy particle patch morphology parameters measured using AFM, from left to right: Particle diameter d (determined in solution using optical microscopy), projected patch diameter d_p , patch arc-angle θ_p , patch height h_p , patch radius of curvature R_p .

II. PARTICLE DYNAMICS AT THE SURFACE

To determine the underlying diffusion time scale of the sedimented particles, we measured their mean-square displacement. The resulting MSD as a function of time (Fig. 2) shows a diffusive power law as expected, but with a diffusion coefficient $D = 0.035 \pm 0.005 \mu\text{m}^2/\text{s}$, a factor of 2 smaller than the bulk diffusion coefficient $D_{einstein} = kT/6\pi r_A \eta = 0.074 \mu\text{m}^2/\text{s}$, where we have used the solvent viscosity $\eta = 1.9\text{mPas}$ for the binary mixture at $T = 30 \text{ C}^\circ$ [2].

For a particle-surface separation smaller than the particle radius, diffusion is expected to slow down significantly. Due to hydrodynamic particle-wall interactions, the diffusion coefficient should decrease according to [3]

$$D = D_{einstein} \left(1 - \frac{8}{15} \ln(1 - \beta) + 0.029\beta + 0.04973\beta^2 - 0.1249\beta^3 \right)^{-1}, \quad (1)$$

where $\beta = r/h$ and h the height of the particle center. Fitting this equation we find $h - r = 0.2 \mu\text{m}$, which is close to the gravitational height of the particles, and presents an effective average height of the particles.

III. FOURIER ANALYSIS

The decomposition of chain bending fluctuations in Fourier modes is provided by eq. 1 in the manuscript. The equation is similar to the expression for continuous filament, with the only difference that we use a discrete Fourier transform. We note that the mode $n = 0$ is merely a global chain orientation, and is not considered in the manuscript, while $n = 1, 2, 3$ etc. correspond to bending fluctuations of increasing order.

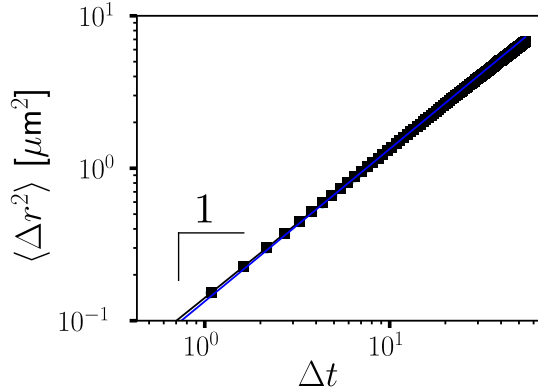


FIG. 2. Diffusion dynamics of individual DP-A particles. The mean square displacement is averaged over 300 particles. Blue line is a fit to the 2D diffusion power law, $\langle \Delta r^2 \rangle = 4D\Delta t$.

The mode inaccuracy as a consequence of the locating error ϵ follows the relation [4]

$$\sigma_{noise}^2(\alpha_q) = \frac{4}{L_0} \epsilon^2 [1 + (N - 2) \sin^2(n\pi/2(N - 1))]. \quad (2)$$

IV. TRANSVERSE AND LONGITUDINAL CHAIN DRAG COEFFICIENTS

The bending relaxation dynamics of a chain is expected to be, at least partly, connected to the diffusion dynamics of the center of mass (COM) of the chain. We can use the exact same data as was used to study the bending dynamics to also determine the COM diffusion. For a semiflexible chain it is convenient to separate COM diffusion into two components: a transversal and a longitudinal diffusion, see Fig. 3(a). To determine the mean square displacement in both directions, first the coordinate system at each frame was rotated by the average tangent angle $\langle \phi \rangle_i$ at that frame. In this way the x-axis coincides with the longitudinal direction and the y-axis with the transversal direction, such that $MSD_{COM}^T = MSD_{COM,x}$ and $MSD_{COM}^L = MSD_{COM,y}$. The resulting mean square displacement of the $N = 15$ chain used for most of the analysis in this chapter is shown in Fig 3(b). Good fits are obtained with diffusive relations $MSD_{COM}^T = 2D^T \Delta t$ and $MSD_{COM}^L = 2D^L \Delta t$. A significantly faster diffusion is obtained in the longitudinal direction which is to be expected for a linear object. We extract the associated drag coefficients per unit length $\gamma_{COM}^T = kT/(D_T N d)$ and $\gamma_{COM}^L = kT/(D_L N d)$, where d is the particle diameter, see Fig. 3(c). Note that we here normalise by the distance between the two tips $L'_0 = N d$ of the chain rather than the distance between the centers of the two end particles $L_0 = N d$. No significant

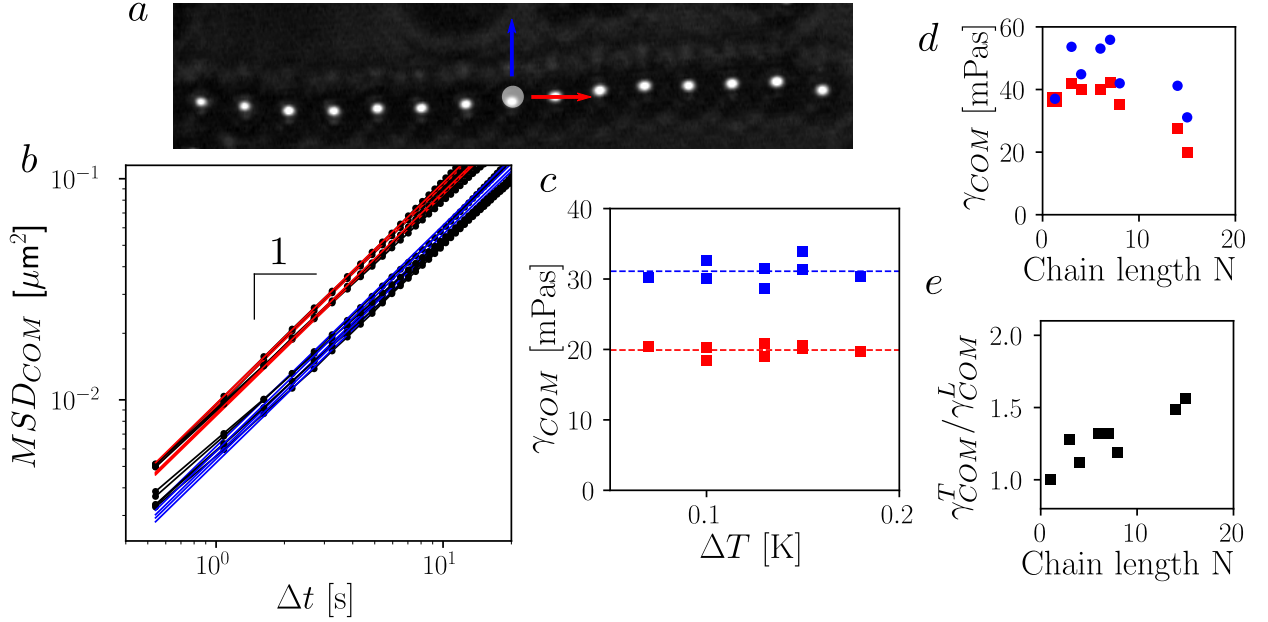


FIG. 3. Transverse (blue) and longitudinal (red) diffusion and associated drag coefficient of dipatch chains (a) Snapshot of the $N = 15$ big-patch chain with center of mass (white transparent dot) and the two diffusion directions (b) mean square displacement and linear diffusive fits at different temperatures. (c,d) The extracted drag coefficients per unit length as a function of temperature with fixed length $N = 15$ and length with fixed $\Delta T = 0.15\text{K}$. (e) Ratio of transverse and longitudinal drag coefficients as a function of chain length

dependence on temperature is observed, which also means the bending rigidity range that is explored here does not alter diffusivity, in line with Ref. [5]. We average all temperatures to obtain the best estimates $\gamma_{COM}^T = 31 \pm 3$ mPas and $\gamma_{COM}^L = 20 \pm 1$ mPas. From the absence of a temperature dependence we further can conclude that there is no significant critical Casimir attraction between particles and wall, which, if present, would give rise to an apparent increase in the drag coefficient with increasing temperature.

We have likewise extracted the center of mass drag coefficients for chains of different sizes and normalized by the chain length, see Fig. 3(d,e). These normalised drag coefficients appear to be fairly consistent over different chain sizes though appear to decrease for longer chains. In addition, a clear trend towards a larger constant between transversal and longitudinal diffusion is observed, which is to be expected due to the increased asymmetry in length.

V. ANALYSIS OF SLOW RELAXATION

In order to model the secondary slower relaxation we use the same analysis strategies as used in ref. [6], which are generally valid in the presence of internal friction. In this case the Langevin dynamics of a filament is modified with an additional dissipatory term:

$$B \frac{\partial^4 u}{\partial s^4} + \gamma \frac{\partial u}{\partial t} + \gamma' \frac{\partial}{\partial t} \left(\frac{\partial^4 u}{\partial s^4} \right) = f(s, t). \quad (3)$$

The third term represents internal friction with internal friction coefficient γ' . Solving this case, the equation for the relaxation time becomes modified to Eq. 7 of the main text. This equation implies that at wave vectors larger than $q_c \sim (\gamma/\gamma')^{1/4}$, internal friction will dominate and correspondingly the relaxation times become q_* -independent and equal to $\tau_c = \gamma'/B$.

VI. SECONDARY RELAXATION IS PRESENT ON SINGLE BOND LEVEL

To get deeper insight into the origin of the slow relaxation we look at three bonded particles only. Three dipatch particles together form effectively a single dipolar bond parametrized by a single bending angle θ , see Fig. 4(a). An overdamped elastic dipolar bond with energy $U(\theta) = k_\theta \theta^2/2$ follows the dynamics

$$\dot{\theta} = -\frac{k_\theta}{\gamma_\theta} \theta + \sqrt{\frac{2kT}{\gamma_\theta}} \xi(t) \quad (4)$$

where γ_θ is an effective angular friction coefficient. This equation is completely analogous to a particle in a harmonic well with the lateral displacement replaced by θ . It is thus similarly solved by the MSD [7]

$$\langle \theta^2 \rangle = 2 \left(1 - e^{-t/\tau_\theta} \right) \frac{kT}{k_\theta}, \quad (5)$$

with $\tau_\theta = \gamma_\theta/k_\theta$. We track the centers of a three-particle chain for different temperatures and follow the evolution of the bending angle.

Fig. 4(b) shows the MSD of θ . Interestingly, like the mode dynamics for longer chains, also the dynamics of single bonds shows two relaxation processes. The initial relaxation fits well with Eq. 5. The resulting fit parameter k_θ divided by kT and multiplied by the particle diameter d is shown in Fig. 4(c). This ratio dk_θ/kT is the persistence length a long chain consisting of a series of this single bond would have. We first see that the bond rigidity is

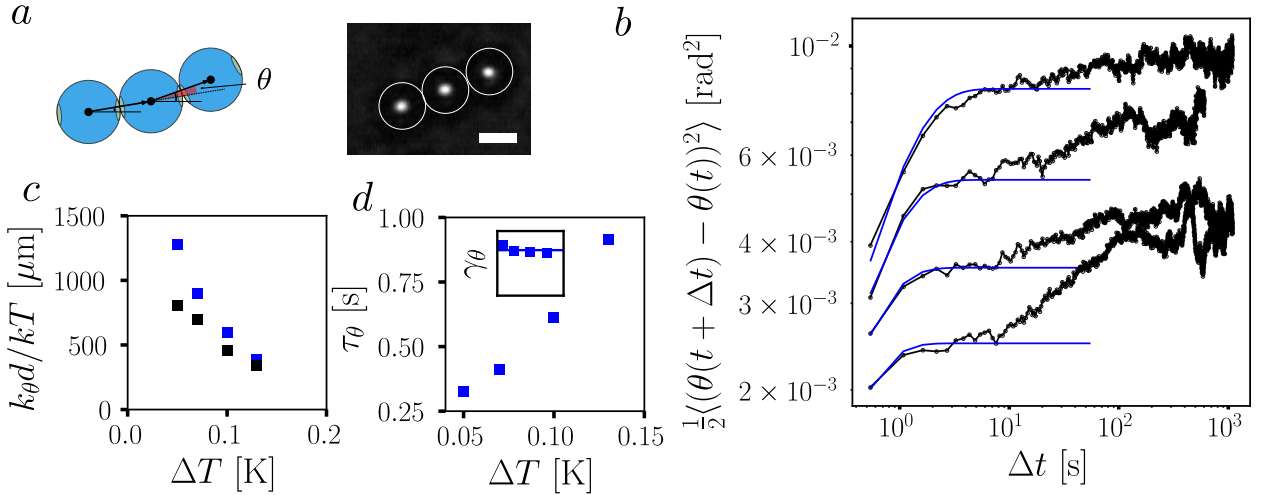


FIG. 4. (a) Model and experimental snapshot of three dipatch particles forming effectively a single dipolar bond, scalebar $3\mu\text{m}$. (b) Mean square displacement of bond angle θ for temperature $\Delta T = 1.3, 1, 0.7, 0.5$ from top to bottom. Blue line is best fitted exponential relaxation on short timescales. (c) Temperature tuneability of fitted bending rigidity on short (blue) and long (black) timescales, normalised to correspond to the persistence length of a chain. (d) Fitted short relaxation time and extracted friction coefficient (inset) with mean value as horizontal line.

tunable with temperature similar to the persistence length of Fig. 5 in the main text. The absolute value is similar, but slightly lower as before. This difference is not surprising given the variability of bond stiffnesses due to particle polydispersity. The fitted relaxation time increases with ΔT , as shown in Fig. 4(d). When we extract γ_{θ} we obtain an almost constant number. The normalised average $\gamma_{\theta}/d^3 = 16 \pm 1$ mPas is comparable to the drag found for free diffusion and in the mode analysis. From this consistent behaviour we conclude that at short timescales a single bond shows elastic overdamped dynamics.

On longer timescales a second relaxation occurs. This relaxation does not fit well with an exponential relaxation (not shown). If we do attempt a fit we obtain a relaxation time $\tau_{slow} = 15 \pm 5\text{s}$, similar to the slow relaxation for chains. Fig. 4(c) shows the effective bending rigidity after this second relaxation. Similar to the long chain also this bending rigidity is temperature tuneable and on the order of a factor two smaller than the short time scale rigidity.

From the overall similarity between long chain and single bond behaviour we conclude that the source of the secondary chain relaxation lies at the single bond level. This allows

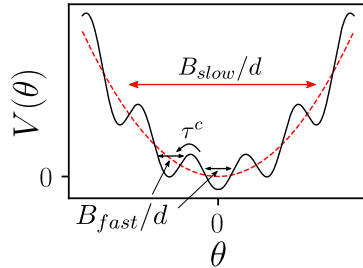


FIG. 5. A potential energy landscape that can model a stick-slip process of the bond angle and qualitatively captures the presence of two bending rigidities B_{fast} and B_{slow} .

us to exclude possible collective effects as the origin, such as longer ranged interactions or hydrodynamic coupling. Furthermore it shows that analysis artifacts due to approximations during the mode analysis are also not the source. In particular the approximation of cosine modes as normal modes does introduce a small mode mixing, with components of long wavelength, slowly decaying modes, also being present in higher modes. Such an artefact could give rise to an apparent second slow relaxation. However given that the secondary relaxation is also present for the three chain, where no mode analysis is done, convincingly shows that this mode mixing artefact is not dominant.

VII. MICROSCOPIC ORIGIN OF NON-ELASTIC RELAXATION

As discussed in the manuscript we speculate that the origin of the internal friction is a stick-slip like process. The source of these stick-slip dynamics could be heterogeneities on the surface such as roughness or charge, or the reptation of intertwined F108 polymer brushes present on the surface. A potential energy landscape that qualitatively captures such behavior is shown in Fig. 5. A valley represents a fixed contact point, with a effective spring bending B_{fast}/d . Due to thermal energy kicks, hopping between valleys can occur leading to contact slippage, which happens on a timescale τ_c . This landscape has in addition a global curvature giving rise to a long time effective bending constant B_{slow}/d . To further show that such a contact point diffusion is in principle possible we note that the average patch size for these particles has been measured directly to be given by a patch arc angle $\theta_p = 0.36\text{rad}$. The explored angle amplitudes are, even on long time scales smaller, $\sim 0.1\text{rad}$, as can be seen from fig. 4(b). If this were not smaller, another mechanism apart from contact

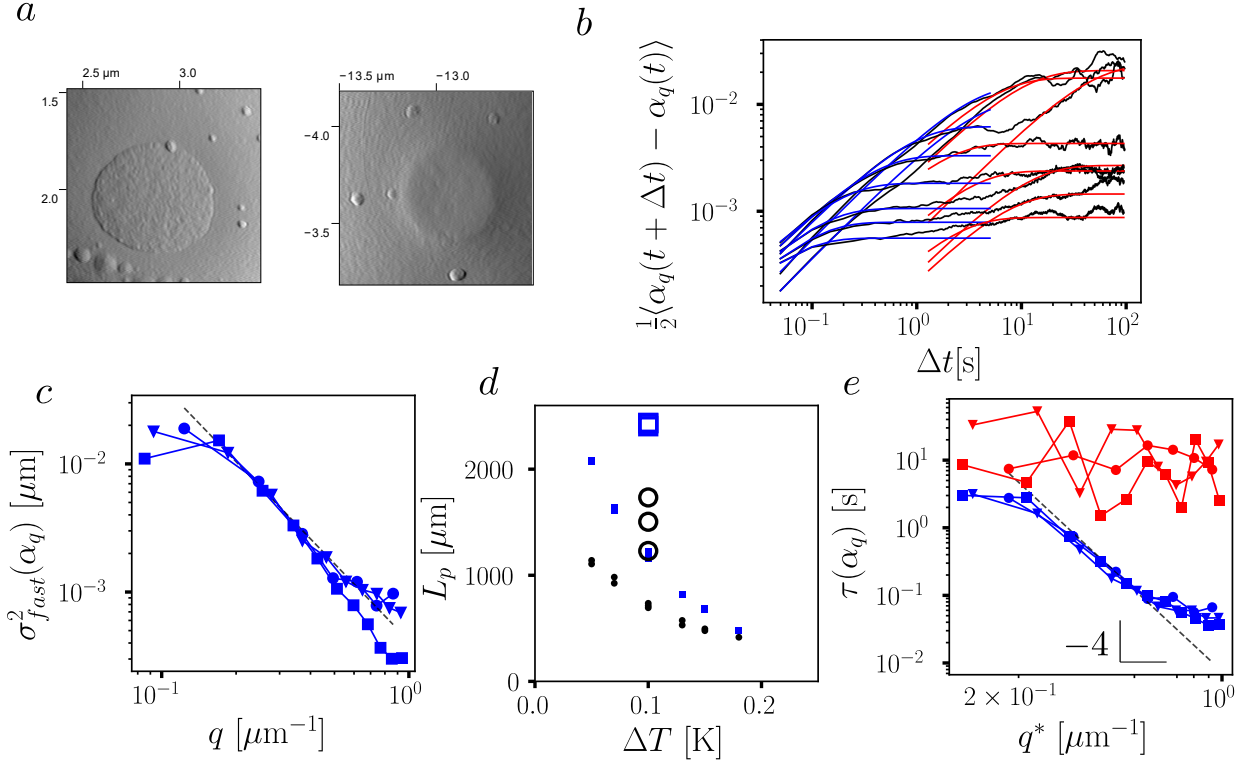


FIG. 6. (a) Atomic force microscope images zoomed in on the patch of large-patch dipatch particles (left) and small-patch (right). (b) Mean square displacement of the lowest modes of a $N = 13$ chain, with exponential relaxation fits on short (blue) and long (red) timescales. (c) Fitted short time mode variance for an $N = 9$, $N = 12$ and $N = 13$ chain, dotted line is q^{-2} powerlaw fit. (d) L_p on short (blue open squares) and long timescales (black open circles), in addition the big patch values are shown. (e) τ_{fast} (blue) and τ_{slow} (red) obtained from the exponential fit, dotted line is a q_*^{-4} fit

diffusion would have to be invoked. However given that this is lower than θ_p it is possible that the explored angle amplitude comes from contact diffusion. There is therefore clearly enough space on the patch to move around and change contact point.

VIII. DEPENDENCE ON PATCH SIZE

Here, we investigate chains of di-patch particles with smaller patches, but otherwise identical properties. Their patch arc angle was $\theta_p = 14^\circ(\pm 2)$ instead of $\theta_p = 21^\circ$. Fig. 6(b) shows the mode mean square displacements of these particles. Also indicated are fits to

two exponential relaxation processes. The higher acquisition rate of these experiments with respect to particle A experiments allow to probe smaller Δt 's and show that also on these shorter timescales the fast relaxation decay fits well. The resulting amplitude of the fast relaxation is shown for three different chains in Fig. 6(c). In all cases a q^{-2} power law is recovered for wavelengths in an intermediate regime. The extracted persistence lengths $L_p^{slow} = 1500 \pm 250 \mu\text{m}$, and $L_p^{fast} = 2420 \pm 20 \mu\text{m}$ are compared with the persistence length of the big patch sample, in Fig. 6(d). Interestingly, both after short and long relaxation the small-patch particle chains exhibit a factor of two higher rigidity.

Fig. 6(e) shows that τ_{fast} follows a q^{-4} dependence from which we fit a drag coefficient of $\gamma = 73 \pm 7 \text{cP}$, very close to the drag coefficient for big patch chains. The slow relaxation time τ_{slow} is within accuracy independent of q , which we average to obtain $\tau_c = 12 \text{s}$, shorter than for the bigger patches. This is consistent with Eq. 7 of the main text, given the fact that B_{slow} is bigger. From τ_c we extract an internal friction coefficient $\gamma' = 0.8 \cdot 10^5 \text{ mPas}\mu\text{m}^4$. This value lies within the error margin of the internal friction of the big patch chains.

These observations highlight the different control parameters in this system. Next to temperature the mechanics of the chains are also tuned by the patch-size, with smaller patches giving more rigid chains. This effects both the overdamped elastic response on short timescales as well as the long time relaxation. The internal friction coefficient however remains unaffected. This indicates that the secondary dissipation mechanism is determined by features set at a length scale smaller than the patch size. These features could be roughness or charge heterogeneities on a length scale smaller than the patch size.

-
- [1] S. G. Stuij, J. Rouwhorst, H. J. Jonas, N. Rufino, Z. Gong, S. Sacanna, P. G. Bolhuis, and P. Schall, “Revealing polymerization kinetics with colloidal dipatch particles,” (2021), arXiv:2106.04346 [cond-mat.soft].
 - [2] Arnold Stein, Steven J. Davidson, Joseph C. Allegra, and Guy F. Allen, “Tracer diffusion and shear viscosity for the system 2,6-lutidine-water near the lower critical point,” J. Chem. Phys. **56**, 6164–6168 (1972).
 - [3] Mauricio D. Carbajal-Tinoco, Ricardo Lopez-Fernandez, and José Luis Arauz-Lara, “Asymmetry in colloidal diffusion near a rigid wall,” Phys. Rev. Lett. **99**, 138303 (2007).

- [4] F. Gittes, B. Mickey, J. Nettleton, and J. Howard, “Flexural rigidity of microtubules and actin filaments measured from thermal fluctuations in shape.” *J. Cell Biol.* **120**, 923 (1993).
- [5] Bipul Biswas, Raj Kumar Manna, Abhrajit Laskar, P. B. Sunil Kumar, Ronojoy Adhikari, and Guruswamy Kumaraswamy, “Linking catalyst-coated isotropic colloids into “active” flexible chains enhances their diffusivity,” *ACS Nano* **11**, 10025–10031 (2017).
- [6] Michael G. Poirier and John F. Marko, “Effect of internal friction on biofilament dynamics,” *Phys. Rev. Lett.* **88**, 228103 (2002).
- [7] Branimir Lukić, Sylvia Jeney, Željko Sviben, Andrzej J. Kulik, Ernst-Ludwig Florin, and László Forró, “Motion of a colloidal particle in an optical trap,” *Phys. Rev. E* **76**, 011112 (2007).